THE JOURNAL OF PHYSICAL CHEMISTRY C
A JOURNAL OF THE AMERICAN CHEMICAL SOCIETY

pubs.acs.org/JPCC

Article

Revealing Intermetallic Active Sites of PtNi Nanocatalysts for Reverse Water Gas Shift Reaction

Hongyu Li,[⊥] Hong Zhang,[⊥] Xuelong Wang, Ralph G. Nuzzo, Anatoly I. Frenkel,* Ping Liu,* and Dilip Gersappe*

Cite This: *J. Phys. Chem. C* 2023, 127, 22067−22075

Read Online

ACCESS | Metrics & More | Article Recommendations | Supporting Information

ABSTRACT: Bimetallic nanoparticles have gained great interest due to their potential applications in catalysis. By combining Lattice Boltzmann Modeling (LBM), Density Functional Theory (DFT) calculations, and kinetic Monte Carlo (KMC) simulation, here we rationalize the superior performance of supported Pt−Ni alloy nanostructures over Pt and Ni alone during the reverse Water Gas Shift (rWGS) reaction, which was observed previously. The LBM simulation including the diffusion and flow of the reacting gas molecules within the supporting nanoporous channels in SBA-15 indicates that the simple combination of contributions from Ni and Pt alone is not enough to result in the observed promotion in rWGS activity and selectivity of the Pt−Ni alloy. Instead, the synergy between Pt and Ni via a unique intermetallic motif is responsible according to the DFT and KMC simulation. Compared to the monometallic counterparts, the intermetallic-introduced ensemble effect at the low-coordinated Pt−Ni hybrid site of Pt−Ni alloy nanocatalysts enables the enhanced activation of CO_2 and promoted removal of CO/H_2O as gas phase product.

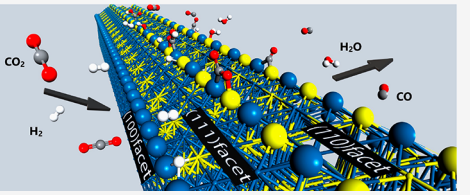

INTRODUCTION

Supported alloy nanocatalysts have a very wide range of chemical and electrochemical applications including reforming processes, water purification, selective hydrogenation/oxidation, and lowering CO_2 emissions.[1−4] Experimental evidence has demonstrated that the effects of the two metal components are often synergistic in nature, and they cannot be expressed by a simple superposition of activities at each metal site.[5−8] This offers an attractive opportunity to depart from the Sabatier principle for improving the activity and selectivity of catalysts. The interplay among the ligand effect (modified electronic structure of metal atoms by alloying), strain effect (modified metal−metal bond length by alloying) and the ensemble effect (modified atomic arrangement at the active sites by alloying) has been proposed to be essential.[9−14] However, rational design of such synergistic catalytic species is currently difficult due to the limited understanding of the geometry and dynamics of these bimetallic catalysts at nanoscale as well as the effects caused by their restructuring in reaction conditions.

To enable the design of bimetallic catalysts, a key challenge is to narrow down the relevant structures of catalytically active species and active sites that are not known a priori due to the large number of possible configurations on the surface of real catalysts. In recent work,[15] we described the operando characterization results obtained during the reverse water gas shift (rWGS) reaction catalyzed by a bimetallic PtNi catalyst supported on the mesoporous silica, SBA-15. The rWGS reaction (eq 1) is the reversible hydrogenation of CO_2 producing CO and H_2O. Experiment shows that the reaction is pressure independent, and according to Le Chatelier's principle, as the reaction is endothermic, it is thermodynamically favored at elevated temperatures. The rWGS reaction is accompanied by CO_2 methanation over the catalysts because of its excessive hydrogenation under ambient pressure. In addition, methanation is exothermic, favored at lower temperatures, as shown in eq 2.

$$CO_2 + H_2 \rightarrow CO + H_2O; \quad \Delta H^{\circ}_{298K} = +41\ \text{kJ/mol} \tag{1}$$

$$CO_2 + 4H_2 = CH_4 + 2H_2O; \quad \Delta H^{\circ}_{298K} = -165\ \text{kJ/mol} \tag{2}$$

One important result emerging from that work, based on the combination of the multimodal characterization tools, was concerned both stoichiometry and intermetallic motifs of the nanoscale Pt−Ni catalyst.[15] It was demonstrated that the catalyst has enhanced selectivity for reduction of CO_2 to CO without significant competitive levels of methanation compared to pure Pt and Ni catalysts supported on SBA-15. A Density Functional Theory (DFT) study using a face centered cubic nanowire (NW) model confirmed that the intermetallic Pt−Ni alloy shows lower potential energy surface than the pure Pt and Ni catalysts for rWGS reaction.[16] That study focused on

Received: August 21, 2023
Revised: October 16, 2023
Accepted: October 17, 2023
Published: November 3, 2023

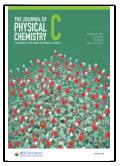

the specific 110/111-edge site, which binds to CO_2 strongly. Yet, the competing behaviors of the other sites and their contributions to the overall rWGS rates of the NW under the reaction condition remains elusive. In addition, the catalyst structure and chemical environments considered in the DFT calculations are too simplified to describe the complex impacts from diffusion and flow of reacting gases through mesoporous framework measured experimentally.

To bridge theory[16] and experiment,[15] a combined modeling approach was conducted to understand how the Pt−Ni bonding framework on the catalyst surface and the flow/diffusion processes within, and on the surface of, nanoporous SBA-15 affect the apparent rWGS rates. We began by estimating the effects of diffusion and flow of the reacting gas molecules within the nanoporous channels in SBA-15 on the apparent rates using the Lattice Boltzmann modeling. This was followed by the DFT calculations and kinetic Monte Carlo (KMC) simulation to describe at an atomic level the catalytic behaviors of different catalytic sites available over a Pt−Ni nanostructure and the corresponding contributions to the overall rate under the rWGS condition. The combination of these theoretical methods at different scales resulted in direct evidence of the essential role that Pt−Ni synergy can play for the enhanced activity and selectivity observed during the rWGS reaction over intermetallic Pt−Ni catalyst.

THEORETICAL METHODS

Lattice Boltzmann Modeling. The Lattice Boltzmann method (LBM) is a meshless method that has been widely used to research on fluid flow in porous materials and can be highly parallelized.[17] Here, space and time were discretized into nodes and intervals by using a regularly spaced lattice geometry. Particles were confined on nodes and are represented by density distribution in different directions (f_i). Applying Bhatnagar, Gross, and Krook (BGK) dynamics, the discrete lattice Boltzmann equation becomes

$$f_i(\boldsymbol{x} + \boldsymbol{e}_i\delta x, t + \delta t) = f_i(\boldsymbol{x}, t) - \frac{\delta t}{\tau}(f_i(\boldsymbol{x}, t) - f_i^{(eq)}(\boldsymbol{x}, t)) \quad (3)$$

where δx and δt are space resolution and time resolution, respectively. In this paper, all LBM timesteps are in lattice unit (δt). $\boldsymbol{e}_i$ is discrete speed of lattice, and τ is the relaxation time. The equilibrium distribution function for convective fluid flow is defined as

$$f_i^{(eq)}(\boldsymbol{x}, t) = w_i\rho\left(1 + \frac{\boldsymbol{e}_i\cdot\boldsymbol{u}}{c_s^2} + \frac{(\boldsymbol{e}_i\cdot\boldsymbol{u})^2}{2c_s^4} - \frac{\boldsymbol{u}^2}{2c_s^2}\right) \quad (4)$$

and for diffusion as

$$f_i^{eq} = w_i\rho\left[1 + \frac{\boldsymbol{e}_i\cdot\boldsymbol{u}}{c_s^2}\right] \quad (5)$$

Here c_s is the speed of sound in the lattice, $\rho = \sum_i f_i$ is local density, $\boldsymbol{u}$ is the macroscopic velocity, and w_i is the weight function for different directions.

In the experiments reported by Liu et al.,[15] the reactant gases CO_2 and H_2 flow into a 6.35 mm inner diameter quartz tube reactor under atmospheric pressure and pass through the catalyst bed. The rates of CO_2 and H_2 coming into the tube are in the 1:2 ratio. The conversion (X), yield (Y) and selectivity (S) are defined using the flow rate of reactant (F, mol/min) as follows:[15]

$$X_{CO_2} = \frac{F_{CO_2}^{inlet} - F_{CO_2}^{outlet}}{F_{CO_2}^{inlet}} \quad (6)$$

$$X_{H_2} = \frac{F_{H_2}^{inlet} - F_{H_2}^{outlet}}{F_{H_2}^{inlet}} \quad (7)$$

$$Y_{CO} = \frac{F_{CO}^{outlet}}{F_{CO_2}^{inlet}} \quad (8)$$

$$Y_{CH_4} = \frac{F_{CH_4}^{outlet}}{F_{CO_2}^{inlet}} \quad (9)$$

$$S_{CO} = \frac{Y_{CO}}{X_{CO_2}} \quad (10)$$

$$S_{CH_4} = \frac{Y_{CH_4}}{X_{CO_2}} \quad (11)$$

To model this system, we needed to develop a chemical reaction model and combine it with LBM which allows us to include kinetic transport. Since our model resolves concentration fields, we adopt an approach in which we model the processes using the overall chemical reaction:

$$aA + bB \rightarrow cC + dD \quad (12)$$

The kinetic equation for this reaction rate takes the form

$$r = kc_A^{n_A}c_B^{n_B} \quad (13)$$

Here n_i is the reaction order in the ith reactant[18] and k is the reaction rate constant. If, at the beginning of the experiment, there are only reactants and no product and the reactant concentrations were in stoichiometric proportions, this expression can be rewritten as follows:

$$-\frac{dc_A}{dt} = k_1c_A^n \quad (14)$$

Here n is the overall reaction order ($n = n_A + n_B$) and

$$k_1 = ka^{1-n_B}b^{n_B} \quad (15)$$

We can examine the overall reaction order and the constant k_1 from the form of the concentration time curve.

$$\frac{1}{(c_A)^{n-1}} = \frac{1}{(c_A^0)^{n-1}} + (n-1)k_1t, \quad \text{for } n \neq 1 \quad (16)$$

and

$$\ln c_A = \ln c_A^0 - k_1t, \quad \text{for } n = 1 \quad (17)$$

We first tested whether we could implement the reaction kinetics into the LBM model by modeling a reaction in a flowing reactor. We used a three-dimensional lattice with periodic boundary conditions in all directions and no obstacle or structure. We coupled the gas velocity field to all components in the simulation, i.e. all components have the same velocity (using the values from the experiments) as they are flowing through the lattice. We initialized A and B using a concentration ratio of 1:1 for A + B → C, and 1:2 for A + 2B → C. The initial concentration of the C component was set to

https://doi.org/10.1021/acs.jpcc.3c05655
J. Phys. Chem. C 2023, 127, 22067−22075

0. The reaction formula (eq 13) was performed at each time step on each lattice node. Our model is shown to be able to recover the correct dynamics (Figures S1 and S2) for the evolution of the reaction, in perfect agreement with analytical predictions. We also confirmed that in the presence of obstacles and limited reaction sites (Supporting Information) our model results matched theoretical predictions.

To simulate the inlet and outlet flow of rWGS according to the experimental conditions, we used the SBA-15 structure and same experimental conditions as reported in ref.[15] The catalyst support SBA-15 has pores that are cylindrical.[19] Based on the paper and the details of the structure, we were able to construct the appropriate LBM structure as shown in Figure 1.

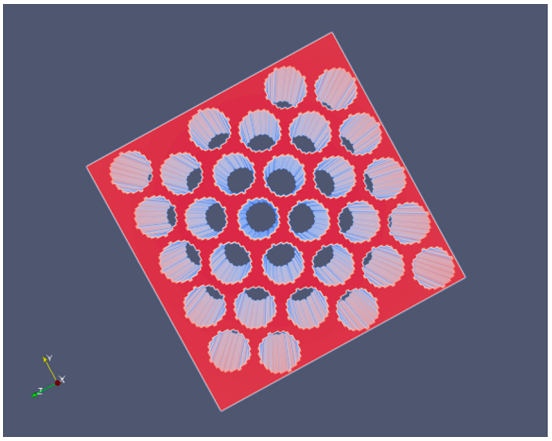

Figure 1. SBA-15 structure model implementation of the LBM lattice.

According to the experimental process,[15] approximately 50 mg of sieved catalysts (40−60 mesh) were used for steady-state experiments. H_2 and CO_2 were set at a 2:1 ratio (10 mL/min H_2 with 5 mL/min CO_2) and diluted with 25 mL/min of Ar. The inlet flow was switched to reactants and held for at least 14 h. The concentrations of gas products were analyzed online by a gas chromatography instrument. In our model, to construct the appropriate boundary condition to generate the same steady inlet flow as experiments, we used bounce-back boundary conditions on SBA-15 boundaries, a fixed density boundary condition at the inlet to give a steady inlet flow at every time step, and Neumann boundary (outflow) condition at the outlet.

The rWGS is a reversible reaction. But in our simulation, the initial concentrations of products are zero, and the reaction does not reach chemical equilibrium. Hence we can view it as a forward reaction instead of a reversible process. Thus, we could derive the reaction rate as

(A) rWGS:

$$r_A = k_1(C_{CO_2})^{\alpha_1}(C_{H_2})^{\beta_1} \quad (18)$$

(B) methanation:

$$r_B = k_2(C_{CO_2})^{\alpha_2}(C_{H_2})^{\beta_2} \quad (19)$$

Table 1 shows the parameters that we needed. The reaction orders α, β are determined by the reaction path, and the value has been determined by the literature.[20,21] The rate constant k is derived by fitting the yield from the simulations to the experiment.

Table 1. Reaction Orders for rWGS and Methanation Reactions from the Literature[20,21] and Rate Constants to Be Fitted

	k_1	α_1	β_1	k_2	α_2	β_2
Pt, monometallic	From fitting	0.70	0.53	From fitting	0.17	0.32
Ni, monometallic	From fitting	0.50	0.82	From fitting	0.17	0.32

Pt is not a good catalyst for CO_2 methanation, which is consistent with experiment. As there is no literature reporting reaction order for the Pt methanation, we assume that it has the same reaction order as Ni. We expect this to be an upper bound on the effect of Pt on methanation. When we reduced this reaction order, no appreciable change was observed in our results. Since our model starts off with only reactants and no product, we run the simulation to achieve steady state by checking our results every 200 timesteps, until our conversion rate does not change. All results reported here are at the steady state.

DFT and KMC Modeling. Following our previous study,[16] Pt_3Ni, Pt, and Ni NWs in 20 Å diameter and octahedral shape were constructed, which were interconnected by the closed-packed facets and described well the experimentally observed difference in chemical property among the three nanostructures (Figure S3). The edge between {111} facets and {100} facets (100/111-edge in our notation) and the edge between {111} facets and {110} facets (110/111-edge) were studied for the rWGS pathway, which was identified as the most active on the NWs by our previous study.[16] In addition, the center of {111} facets (111-terrace) was also included, which corresponds to the larger surface area and thus provides more active sites than {100} and {110} due to its lower surface energy. The clean NWs and NWs with reaction intermediates were relaxed to the most stable configuration, and the adsorption energies of all intermediate species are referenced to the clean NW and gas phase reaction CO_2 and H_2 molecules.

The structural optimization was performed with spin-polarized DFT calculations, using the Vienna Ab Initio Simulation Package (VASP)[22−24] with Perdew−Burke−Ernzerhof (PBE)[25] functional to describe electronic exchange and correlation. A minimum of 15 Å vacuum was placed between adjacent NWs to avoid possible lateral interactions. A 1 × 1 × 2 Monkhorst−Pack grid and first order Methfessel-Paxton with a smearing width of 0.2 eV were used to integrate over Brillouin zone. Structural optimization was finalized at an electronic convergence of 1×10^{-6} eV and ionic convergence of 0.02 eV/Å Hellman−Feynman force on each ion, using the Conjugate Gradient ionic relaxation algorithm[26] and the RMM-DIIS ionic relaxation algorithm[27] with a plane wave cutoff energy of 400 eV.

Climbing image nudged elastic band method (ciNEB)[28−31] were used to search the transition states (TS) between key intermediates of rWGS pathway, the convergence level of each image of the pathway was 0.02 eV/Å in force-based RMM-DIIS algorithms.[27] Saddle points were confirmed by vibrational frequency calculation that was only applied to adsorbate molecules and metal atoms directly interacted with the adsorbates, while other atoms in the system were constrained.

The KMC simulation was performed on a planar matrix, which was presented by a 111-terrace interconnected by a 100/111-edge and 110/111-edge (Figure S4). All active sites were sampled on a 16 × 16 matrix in 100 μs to ensure the

https://doi.org/10.1021/acs.jpcc.3c05655
J. Phys. Chem. C 2023, 127, 22067−22075

Table 2. Results from Fitting the Reaction Parameters and Its Conversion/Yield vs the Experiment Conversion/Yield

	k_1	k_2	CO_2 conversion ($\times 10^{-5}$ %)	H_2 conversion ($\times 10^{-5}$ %)	CO yield ($\times 10^{-5}$%)	CH_4 yield ($\times 10^{-5}$ %)
Pt, simulation	4.29×10^{-9}	1.29×10^{-11}	6.11	3.15	6.03	0.06
Pt, experiment	–	–	6.14	3.28	6.08	0.06
Ni, simulation	6.75×10^{-9}	1.14×10^{-9}	21.25	18.50	15.96	5.50
Ni, experiment	–	–	21.26	19.04	15.96	5.29

steady state, where both the forward and backward reactions were included. For the initial step of rWGS reaction is the activation of CO_2, both Langmuir−Hinshelwood (LH) mechanism and Eley−Rideal (ER) mechanisms was included depending on the binding of CO_2. The LH mechanism followed the collision theory,[32,33] in which the adsorption rate of CO_2 was determined by

$$r_{ads} = \frac{\sigma^0(T,\theta) A_{site} P_{CO_2}}{\sqrt{2\pi m_{CO_2} k_B T}} \exp\left(\frac{-E_a}{k_B T}\right) \tag{20}$$

where r_{ads} is the CO_2 adsorption rate constant. $\sigma^0(T,\theta)$ is the sticking probability which is approximated as 1. A_{site} is the adsorption site area. P_{CO_2} is the partial pressure of CO_2 of 0.1 atm according to the experimental condition.[15] m_{CO_2} is its molecular weight, k_B denotes the Boltzmann constant, T is the temperature, which is constant 673 K in this case, and E_a is the reaction barrier which is 0 in the case of chemisorbed CO_2.

The rate constants in ER mechanism of CO_2 activation and surface reactions were calculated according to the transition state theory:[34]

$$r_c = \frac{k_B T}{h} \exp\left(-\frac{(\Delta G^{TS-IS}_{(T,P)})}{k_B T}\right) \tag{21}$$

The reaction rate r_c is a function of temperature T and activation free energy ΔG, where h denotes the Planck constant. The total free energy of gas phase molecule was calculated as $G^0 = E_0 + \mathrm{ZPE} - \mathrm{TS} + \Delta H_T + k_B T \ln(P_{CO_2}/P_0)$, where for chemisorbed surface species, the last two terms were negligible. The total energy E_0 and zero point energy (ZPE) were calculated from DFT, the entropy TS at T = 673 K was obtained from the NIST Computational Chemistry Comparison and Benchmark Database (CCCBDB)[35] that matched the same level of theory with our calculations. The enthalpy difference $\Delta H_{673\ K}$ was obtained from the NIST-JANAF thermodynamic table,[36] the reference P_0 was 1 atm. We assumed chemisorbed *H was readily available and easy to diffuse on the NWs under the rWGS at 673 K. As reported previously, the dissociative adsorption of hydrogen was facile on both Ni and Pt, the dissociative barriers could be as low as 0.06 eV on Ni and 0.03 eV on Pt surfaces.[37−40] The diffusion barrier of *H was reported to be 0.2 eV on Pt at 100 K[41] and 0.38 eV on Ni at 220−330 K,[42] ensuring the high mobility of *H on the NWs at 673 K. Note that the lateral interactions between the surface species involved in the rWGS condition was not considered, as the contribution to the overall activity was found to be limited by the low coverage according to the KMC results.

To identify the elementary step that controls the overall rWGS activity, sensitivity analysis was performed on the KMC model. Using a finite differential method with five sampling points, we evaluated the sensitivity (T_n) of the overall CO production rate (r) in response to the perturbation of the energy of the nth intermediate or transition state. The details of the method can be retrieved from our previous studies.[33,43]

$$T_n = \frac{1}{r}\left(\frac{\partial_r}{\partial_{E_n}}\right)_{E_{m\neq n}} \tag{22}$$

Results of the LB Modeling. Following the same data analysis methods (eqs 6−9) as in the experiment,[15] we calculated conversion/yield. That allowed us to obtain the range of rate constant values, k, for each catalyst by testing a range of various attempted values and finally converge on a value that has the best fit to the experiment data. According to the experiment, the amount of catalyst could have significant influence on conversion and yield. This is reasonable because the reaction does not reach chemical equilibrium. Hence, the longer SBA-15 channel, the more nanoparticles are located along the flow-direction ($+x$) that gas could contact, the larger is the conversion/yield. Therefore, we use the quantity "conversion/yield per unit length" to compare our results to the experiments. In the experiment a length of 5 mm of catalyst in quartz tube was used. If we simulate a tube with a 50 nm long channel, then the target conversion/yield would be a factor of 10^5 smaller than the experimental conversion/yield. Table 2 shows the fitted parameter and its conversion/yield versus experiment conversion/yield. We also ran a simulation to confirm our assumption that conversion is linear with tube length is reasonable for this system and a doubling of the tube length leads to a doubling of the conversion and yield as expected. The results are shown in Table S1.

Finally, using the fitted values for the Pt and Ni catalysts we then designed the reaction in Pt−Ni bimetallic catalyst as a simple mixture of Pt and Ni to check whether the overall reaction is based on a simple mixing effect. Based on the semiquantitative schematic model reported in the literature, there are 37 atoms in a single nanoparticle. Twenty-seven of 37 are on the surface and are accessible for gas molecules.[15] 15 out of 27 surface atoms are Pt (56%), another 12 are Ni (44%). If there is no synergy between Pt and Ni, the Pt−Ni bimetallic nanoparticle should have 55.56% catalysis ability of Pt, and 44.44% catalysis ability of Ni. This should be reflected on the value of rate constant, k. Using the values of the fitted k_1 and k_2 (Table 2), we then simulated a Pt−Ni bimetallic system assuming no synergy between them, and we could compare the experiment result and our simulation result under the no synergy. As shown in Figure 2, only few combinations give selectivity more than 10, and no combination has selectivity even at the same order of magnitude as the experimental results reported.[15,16] This seems to strongly indicate that any proportion of a simple combination of Pt and Ni cannot result in both high yield and high selectivity as in the experiment, and therefore, a synergistic effect must take place in this bimetallic catalyst.

DFT and KMC Results for the rWGS Reaction over Ni, Pt and Pt_3Ni Nanocatalysts. As indicated above, the superior behaviors of Pt−Ni alloy nanocatalysts observed

https://doi.org/10.1021/acs.jpcc.3c05655
J. Phys. Chem. C 2023, 127, 22067−22075

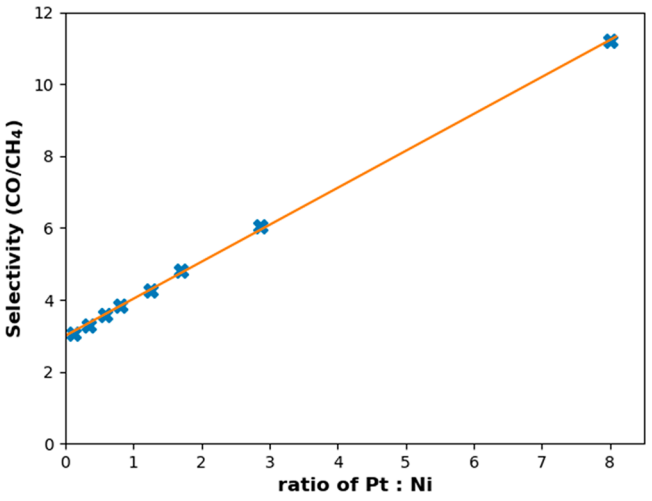

Figure 2. Predicted selectivity of different Pt−Ni linear combinations. The red line is drawn to show the trend.

experimentally for the rWGS reaction cannot be described by the simple combination of Pt and Ni in spite of including the description of diffusion and flow of reacting gases wihin the supporting SBA-15 in the LB model. Thus, we hypothesize that at atomic level the active site should feature some kind of synergy between Pt and Ni in their bimetallic form. Wherein, the ligand, strain and ensemble effects were considered to pinpoint the promoting mechanism of Pt_3Ni over Ni and Pt alone.

We previously screened the CO_2 and CO adsorption on both Pt_3Ni and single metal NWs with the same size and shape using DFT, and considered the rWGS reaction at the site of strongest CO_2 adsorption: 110/111-edge on Pt_3Ni and 100/111-edge on the single metal NWs.[16] On Pt_3Ni, the active site is featured with the unique single atom Ni surrounded by Pt at the low-coordinated edge, being able to enhance the chemisorption of CO_2 and the C−O bond cleavage by ensemble effect but weakening the binding of *OH and *CO by ligand and strain effect to promote the productions of CO and H_2O. However, these studies only considered the reaction at the strongest CO_2 adsorption site, the overall activities of NWs under reactive conditions and the actual rate limiting steps remain elusive.

Here, we calculated the potential energy diagram of rWGS using DFT at both types of edges and the 111-terraces on each NW via a typical reaction pathway (Figure 3 and Table S2−S4) including:[15,44] (1) CO_2 adsorption as $*CO_2$; (2) Activation of CO_2 to the carboxyl *HOCO intermediate via either the Langmuir−Hinshelwood (L−H) mechanism or the Eley−Rideal (E−R) mechanism; (3) *HOCO scission into carbon monoxide *CO and hydroxyl *OH; (4) *CO desorption; (5) *OH elimination by hydrogenation to water $*H_2O$; and (6) desorption of $*H_2O$. The overall reaction rate of entire NW under the experimental conditions was then predicted by combining with KMC simulation. According to the desorption rate of CO produced from the rWGS reaction at the steady states (Figure 4), among the three types of sites considered (e.g., 100/111-edge, 110/111-edge, and 111-terrace, Figure S2) the lower coordinated edges are more active to drive the rWGS reaction instead of the terraces for Pt, Ni, and Pt_3Ni NWs. Specifically, the 100/111-edge is identified as the most active site for Pt and Ni, which is followed by 110/111-edge and 111-terrace in a decreasing sequence. While on

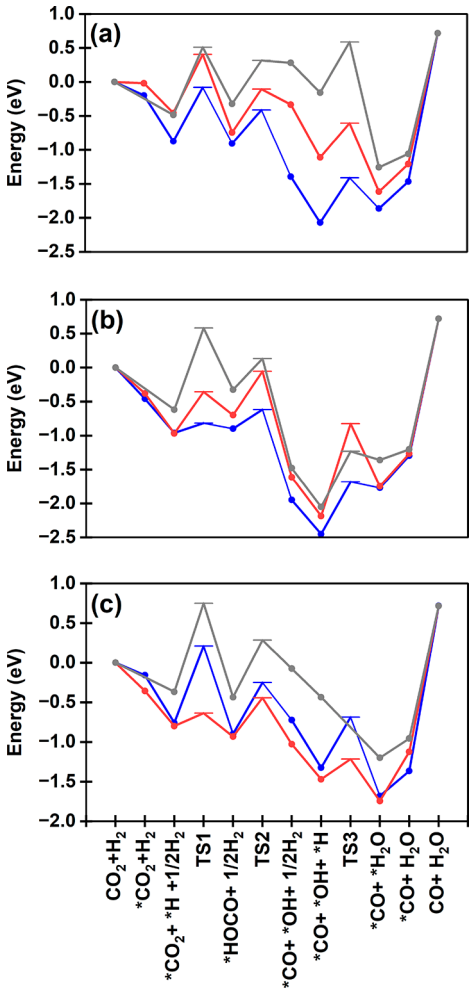

Figure 3. Potential energy diagram for the rWGS pathway on (a) Pt NW, (b) Ni NW, and (c) Pt_3Ni NW. Blue: 100/111-edge. Red: 110/111-edge. Gray: 111-terrace.

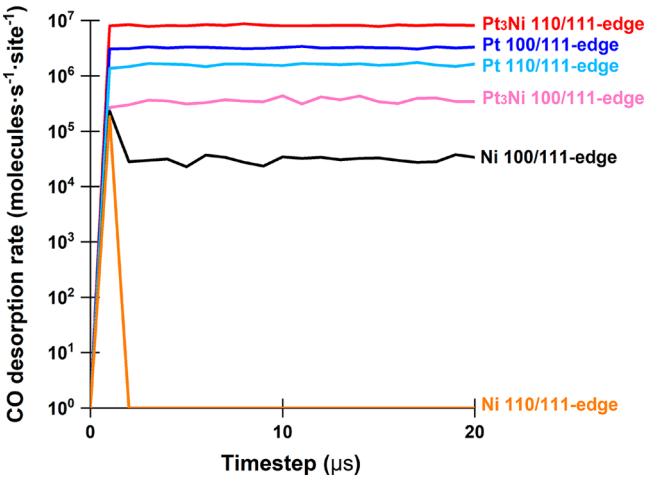

Figure 4. KMC-simulated CO desorption rate (molecules·site^{-1}·s^{-1}) from the step edges during the rWGS on Ni, Pt, and Pt_3Ni NWs at 673 K.

Pt_3Ni the rWGS activity decreases going from 110/111-edge, 100/111-edge, and 111-terrace (Tables S2−S4). The most active 110/111-edge on Pt_3Ni NW provides the *CO desorption rate of 8.19×10^6 molecules·site^{-1}·s^{-1}, which is

https://doi.org/10.1021/acs.jpcc.3c05655
J. Phys. Chem. C 2023, 127, 22067−22075

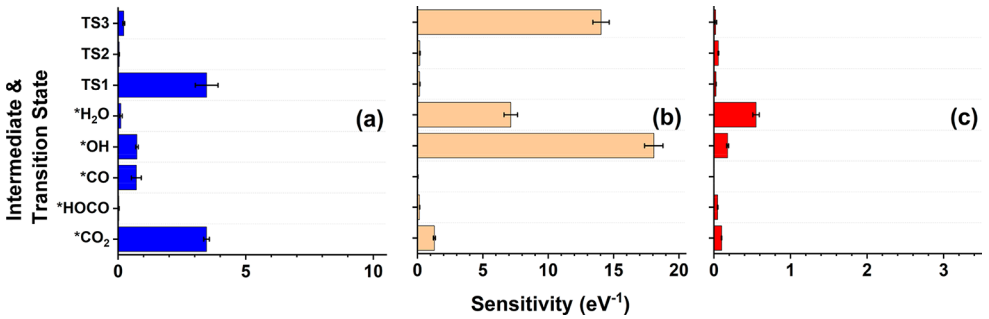

Figure 5. Sensitivity analysis of CO production rate based on the developed KMC model at the most active site: (a) Pt NW 100/111-edge, (b) Ni NW 100/111-edge, and (3) Pt_3Ni NW 110/111-edge. Longer bar indicates higher sensitivity of CO production rate in response to the perturbation in energy of intermediate or transition state. The error bar presents the uncertainty of the finite difference derived from 5 discrete data points.

decreased by 2.5 times on Pt NW and 400 times on Ni NW with the 100/111-edge as the most active site (Figure 4).

According to the KMC results, the contribution from the most active sites is found to dominate the overall CO production on Pt_3Ni (95.3%) and Ni (100%) NWs. By comparison, it decreases to 66.6% for Pt NW, where the secondary active site, the 110/111-edge, also potentially contributed (33.4%). The DFT results show that the 110/111-edge of Pt NW behaves similarly to the 100/111-edge (Figure 4) with the CO desorption rate slightly differing according to the KMC simulation, while a more significant drop in rate going from the most active to other sites was observed for Pt_3Ni and Ni NWs. The preference in rWGS activity at the most active site, 100/111-edge than that at the secondary active site, 110/111-edge, of Pt NW is related to the strain effect. The 100/111-edge of Pt NW shows higher structural fluxionality than 110/111-edge, which helps to accommodate chemisorbed species. No contribution from the 111-terrace is observed for three NW systems due to not only the higher enthalpic barrier of CO_2 activation via the E-R mechanism than that via the L-H mechanism at the edges, but also the additional entropic contrition for gas phase CO_2[35] at 673 K. Nevertheless, the overall sequence in rWGS activity including the contributions from both step edges and 111-terrace remains the same as that only from the most active edge sites: Pt_3Ni > Pt > Ni. Therefore, the most active sites are adequate to demonstrate the synergy between Pt and Ni in bimetallic form, which are considered for mechanistic understanding as follows.

The predicted sequence in rWGS activity based on DFT calculations and KMC simulation not only agrees well with the observed trend for the monometallic systems in the experiment and LB modeling, but also captures the superior activity of the bimetallic over the monometallic systems. More importantly, it can pinpoint the origin of the promoting effect of the bimetallic system, which is essential for the further development of bimetallic-derived catalysts for the rWGS reaction. According to the results of DFT and KMC simulation, the intermetallic Pt−Ni synergy in Pt_3Ni to promote the rWGS activity is rather complex. Depending on the type of intermediates and elementary step, the interplay among ligand, strain, and ensemble effects can make the alloy behave like Ni or Pt, or differently (between Ni and Pt, or beyond Pt and Ni), and the combination leads to the superior rWGS activity over Ni and Pt.

Sensitivity analysis was performed at the most active site, 100/111-edge for Pt NW, 100/111-edge for Ni NW, and 110/111-edge for Pt_3Ni NW, aiming to identify the rate-controlling step following our previous studies.[33,43] The results show that the rate-controlling steps differ among the three systems. Both $*CO_2$ adsorption and its hydrogenation to *HOCO (TS1) are identified as the rate-controlling steps for the rWGS reaction over Pt (Figure 5a). Specifically, the rWGS rate can benefit from enhanced binding of $*CO_2$ and lowered reaction barrier to form *HOCO. While in the case of Ni (Figure 5b), the increase in the CO production rate dominantly depends on the weakened *OH binding with the lowered barrier for sequential hydrogenation to $*H_2O$ (TS3) as the secondary. By contrast, on Pt_3Ni (Figure 5c) no obvious rate-limiting step is identified. Wherein, the binding energy of $*H_2O$ contributes slightly more than the others, but it is much less significant than the rate-controlling steps identified for Pt and Ni, thus a faster rWGS is observed (Figure 4).

Compared to Pt, the promoted rWGS rate on Pt_3Ni is associated with the enhanced binding of $*CO_2$ (adsorption energy or E_{ads} = −0.30 eV for Pt_3Ni, −0.20 eV for Pt) and lowered reaction barrier to form *HOCO (TS1: activation barrier or E_a = 0.16 eV for Pt_3Ni, 0.79 eV for Pt, Table S2), so that these steps do not limit the overall rWGS conversion anymore (Figure 5). While the weakened *OH binding (E_{ads} = 0.10 eV for Pt_3Ni, −0.65 eV for Ni) and the facilitated elimination of *OH in the form of H_2O on Pt_3Ni (TS3: E_a = 0.22 eV for Pt_3Ni, 0.95 eV for Ni, Table S2) are responsible for the higher rWGS activity than Ni (Figure 4).

The promoting effect of bimetallic Pt_3Ni as compared to parent monometallic Pt and Ni depends on the alloy-introduced variation in the active site (Figure S5), binding property (Figure 3), and reaction kinetics (Figures 5). The ensemble effect introduces the Ni single atom site at the most active 110/111-edge, where Pt and Ni act as active anchors for C and O, respectively (Figure S5). According to the calculated the partial density of states (PDOS) of the adsorption sites, with the higher-lying d-band center (ε_d) of Ni (ε_d = −1.51 eV, Table S5) at the 110/111-edge of Pt_3Ni than that of Pt (ε_d < −2.40 eV, Table S5), the electron back-donation from Ni site to asymmetry O 2π* of CO_2 is more significant according to the d-band theory,[45,46] being able to stabilize the molecule more and facilitate the sequential hydrogenation to *HOCO on Pt_3Ni. Yet, it is not as significant as that of pure Ni due to the lack of high symmetric Ni sites.[45−48]

The high-lying ε_d of Ni (ε_d = −1.61 eV, Table S5) at the 100/111-edge of Ni enables the strongest binding to the reaction intermediates including CO_2 among the three systems studied (E_{ads} = −0.44 eV for CO_2, Figure 3). However, a much lower amount of $*CO_2$ is converted to *CO as compared to Pt and Pt_3Ni (Figure 4). This is associated with the overstabilized

https://doi.org/10.1021/acs.jpcc.3c05655
J. Phys. Chem. C 2023, 127, 22067−22075

*OH, and thus difficult removal, which hinders the overall rWGS reaction (Figure 5). It causes the high accumulation of *OH on edge sites of Ni NW (Figure 6), which reaches 0.5

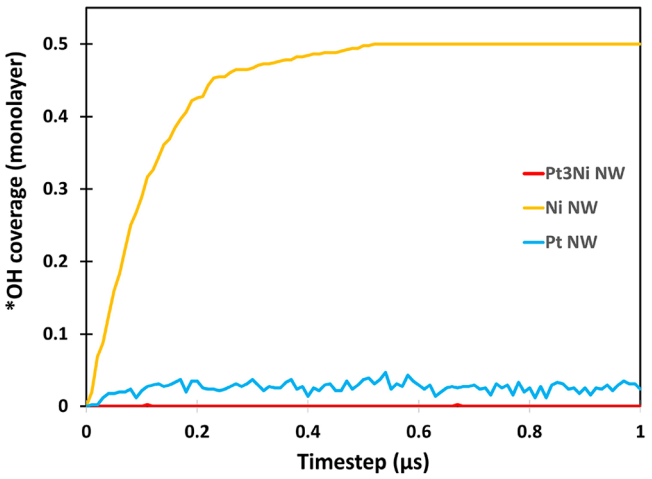

Figure 6. KMC-simulated *OH concentration accumulation during the rWGS reaction on edge sites of Ni, Pt, and Pt_3Ni NWs at 673 K.

monolayer (ML) of coverage. As a result, a drastic drop of rWGS activity to zero is observed at the 110/111-edge (Figure 4) due to the highly difficult *OH removal (E_a = 1.36 eV, Figure 3b). While the most active 100/111-edge sites of Ni are also poisoned by *OH, *OH can be slowly removed with a lower barrier (E_a = 0.95 eV) followed by a facile *H_2O desorption (E_a = 0.47 eV). Yet the CO desorption rate and the overall rWGS activity is much lower than Pt and Pt_3Ni (Figure 4). No *OH accumulation is observed for Pt_3Ni (Figure 6), where *OH prefers the Pt−Ni hybrid bridge at the 110/111-edge instead of high Ni symmetric sites as seen for Ni alone (ensemble effect, Figure S5).[16] Thus, although a direct Ni−OH bond is formed, the binding of *OH (E_{ads} = 0.10 eV, Table S5) is weakened and the *OH removal is facilitated (E_a = 0.22 eV). The slightly lower coverage of *OH observed for Pt_3Ni than Pt (Figure 6) is associated with the direct participation of a single Ni atom (ensemble effect) to stabilize TS3 more significantly and thus lower the reaction barrier (E_a = 0.22 eV for Pt_3Ni, 0.41 eV for Pt). Note that, the strain and ligand effects introduced by forming Pt−Ni alloy also contribute by tuning the stability of reaction intermediates and transition states, yet it is less significant than the contribution from the ensemble effect as demonstrated previously.[16]

Overall, Pt can carry out the rWGS reaction at both the 100/111-edge and 110/111-edge, though the conversion can be limited due to the weak CO_2 binding. Ni alone can bind CO_2 strongly and hydrogenate CO_2 actively at both edges, while it interacts with *OH species too strongly, which leads to the complete or partial poisoning of active sites and hinders the overall reaction. The alloy outperforms both monometallic systems via the single Ni site surrounded by Pt at the 110/111-edge, being active enough to stabilize *CO_2 and facilitate the further hydrogenation but still moderate enough to allow the facile removal *OH and prevent the surface poisoning. Here, the promoting effect by forming Pt−Ni alloy strongly depends on the ensemble effect intermediate and transition state species. The contribution from strain and ligand effects is relatively subtle. We note that this combined multiscale modeling methodology may be helpful for explaining enhanced activity and stability in other intermetallic systems, such as recently reported intermetallic PtNiN catalysts.[49]

CONCLUSIONS

A combined multiscale modeling was performed to rationalize the synergistic effects in multicomponent catalytic systems, where the promoted activity and selectivity, observed previously, during the rWGS reaction over a Pt−Ni bimetallic nanocatalyst were taken as a case study. First, the experimental system including the diffusion and flow of reacting gas molecules within the supporting nanoporous channels of SBA-15 was simulated using the LBM and a good match between the theoretical and experimental yields for Ni and Pt catalysts alone was obtained. However, the linear combination of contributions from Ni and Pt alone was found to be not enough to result in the observed promotion in the rWGS activity and selectivity of the Pt−Ni alloy, and the Pt−Ni synergy could be necessary. Indeed, a combined DFT and KMC simulation on a NW model revealed the superior rWGS activity of the Pt−Ni alloy NW over the monometallic parents via the synergy between Pt and Ni. The alloy can take advantage of each parent monometallic system to promote activity and selectivity via the single Ni site surrounded by Pt at the 110/111-edge introduced by the ensemble effect. The multiscale methodology presented here can be easily extended for screening other bimetallic and multimetallic catalytic systems for possible synergistic effects related to their activity and selectivity in heterogeneously catalyzed reactions.

ASSOCIATED CONTENT

Supporting Information

The Supporting Information is available free of charge at https://pubs.acs.org/doi/10.1021/acs.jpcc.3c05655.

Supplementary figures and tables, including the LB, DFT, and KMC models; *CO_2 adsorption configurations; and DFT calculated reaction parameters and energetics (PDF)

AUTHOR INFORMATION

Corresponding Authors

Anatoly I. Frenkel − *Department of Materials Science and Chemical Engineering, Stony Brook University, Stony Brook, New York 11794, United States; Chemistry Division, Brookhaven National Laboratory, Upton, New York 11973, United States;* orcid.org/0000-0002-5451-1207; Email: anatoly.frenkel@stonybrook.edu

Ping Liu − *Department of Materials Science and Chemical Engineering, Stony Brook University, Stony Brook, New York 11794, United States; Chemistry Division, Brookhaven National Laboratory, Upton, New York 11973, United States;* orcid.org/0000-0001-8363-070X; Email: pingliu3@bnl.gov

Dilip Gersappe − *Department of Materials Science and Chemical Engineering, Stony Brook University, Stony Brook, New York 11794, United States*; Email: dilip.gersappe@stonybrook.edu

Authors

Hongyu Li − *Department of Materials Science and Chemical Engineering, Stony Brook University, Stony Brook, New York 11794, United States*

https://doi.org/10.1021/acs.jpcc.3c05655
J. Phys. Chem. C 2023, 127, 22067−22075

Hong Zhang − *Department of Chemistry, Stony Brook University, Stony Brook, New York 11794, United States*
Xuelong Wang − *Chemistry Division, Brookhaven National Laboratory, Upton, New York 11973, United States*
Ralph G. Nuzzo − *Department of Chemistry, University of Illinois, Urbana, Illinois 61801, United States*

Complete contact information is available at: https://pubs.acs.org/10.1021/acs.jpcc.3c05655

Author Contributions

[⊥]H.L. and H.Z. contributed equally to this work.

Notes

The authors declare no competing financial interest.

■ ACKNOWLEDGMENTS

A.I.F. and R.G.N. acknowledge support of the U.S. Department of Energy, Office of Science, Office of Basic Energy Sciences (U.S. DOE BES), Grant No. DE-SC0022199. The DFT and KMC studies were carried out at Brookhaven National Laboratory (BNL) and supported by the division of Chemical Science, Geoscience, and Bioscience, Office of Basic Energy Science of the US Department of Energy (DOE) under Contract No. DE-SC0012704, using computational resources at Center for Functional Nanomaterials (CFN), a component of the Computational Science Initiative at BNL, and the high-performance SeaWulf computing system of Stony Brook Research Computing and Cyberinfrastructure and the Institute for Advanced Computational Science at Stony Brook University, which was made possible by a National Science Foundation grant (No. 1531492).

■ REFERENCES

(1) Xie, Z.; Winter, L. R.; Chen, J. G. Bimetallic-Derived Catalysts and Their Application in Simultaneous Upgrading of Co2 and Ethane. *Matter* **2021**, *4*, 408−440.
(2) Wong, M. S.; Alvarez, P. J. J.; Fang, Y.-l.; Akçin, N.; Nutt, M. O.; Miller, J. T.; Heck, K. N. Cleaner Water Using Bimetallic Nanoparticle Catalysts. *J. Chem. Technol. Biotechnol.* **2009**, *84*, 158−166.
(3) Lee, J. D.; Miller, J. B.; Shneidman, A. V.; Sun, L.; Weaver, J. F.; Aizenberg, J.; Biener, J.; Boscoboinik, J. A.; Foucher, A. C.; Frenkel, A. I.; et al. Dilute Alloys Based on Au, Ag, or Cu for Efficient Catalysis: From Synthesis to Active Sites. *Chem. Rev.* **2022**, *122*, 8758−8808.
(4) Ghosh Chaudhuri, R.; Paria, S. Core/Shell Nanoparticles: Classes, Properties, Synthesis Mechanisms, Characterization, and Applications. *Chem. Rev.* **2012**, *112*, 2373−2433.
(5) Singh, A. K.; Xu, Q. Synergistic Catalysis over Bimetallic Alloy Nanoparticles. *ChemCatChem.* **2013**, *5*, 652−676.
(6) Basnet, P.; Kc, S.; Dhungana, R. K.; Shrestha, B.; Boyle, T. J.; Giri, R. Synergistic Bimetallic Ni/Ag and Ni/Cu Catalysis for Regioselective γ,δ-Diarylation of Alkenyl Ketimines: Addressing B-H Elimination by in Situ Generation of Cationic Ni(Ii) Catalysts. *J. Am. Chem. Soc.* **2018**, *140*, 15586−15590.
(7) Sha, J.; Paul, S.; Dumeignil, F.; Wojcieszak, R. Au-Based Bimetallic Catalysts: How the Synergy between Two Metals Affects Their Catalytic Activity. *RSC Adv.* **2019**, *9*, 29888−29901.
(8) Prati, L.; Villa, A.; Jouve, A.; Beck, A.; Evangelisti, C.; Savara, A. Gold as a Modifier of Metal Nanoparticles: Effect on Structure and Catalysis. *Faraday Discuss.* **2018**, *208*, 395−407.
(9) Liu, P.; Norskov, J. K. Ligand and Ensemble Effects in Adsorption on Alloy Surfaces. *Phys. Chem. Chem. Phys.* **2001**, *3*, 3814−3818.
(10) Zhang, X.; Yu, S.; Qiao, L.; Zheng, W.; Liu, P. Stabilization of Pt Monolayer Catalysts under Harsh Conditions of Fuel Cells. *J. Chem. Phys.* **2015**, *142*, 194710.
(11) Zhang, X.; Yu, S.; Zheng, W.; Liu, P. Stability of Pt near Surface Alloys under Electrochemical Conditions: A Model Study. *Phys. Chem. Chem. Phys.* **2014**, *16*, 16615−16622.
(12) Gao, F.; Goodman, D. W. Pd−Au Bimetallic Catalysts: Understanding Alloy Effects from Planar Models and (Supported) Nanoparticles. *Chem. Soc. Rev.* **2012**, *41*, 8009−8020.
(13) Zhang, S.; Tang, Y.; Nguyen, L.; Zhao, Y.-F.; Wu, Z.; Goh, T.-W.; Liu, J. J.; Li, Y.; Zhu, T.; Huang, W.; et al. Catalysis on Singly Dispersed Rh Atoms Anchored on an Inert Support. *ACS Catal.* **2018**, *8*, 110−121.
(14) Wang, Y.; Cao, L.; Libretto, N. J.; Li, X.; Li, C.; Wan, Y.; He, C.; Lee, J.; Gregg, J.; Zong, H.; et al. Ensemble Effect in Bimetallic Electrocatalysts for CO_2 Reduction. *J. Am. Chem. Soc.* **2019**, *141*, 16635−16642.
(15) Liu, D.; Li, Y.; Kottwitz, M.; Yan, B.; Yao, S.; Gamalski, A.; Grolimund, D.; Safonova, O. V.; Nachtegaal, M.; Chen, J. G.; et al. Identifying Dynamic Structural Changes of Active Sites in Pt−Ni Bimetallic Catalysts Using Multimodal Approaches. *ACS Catal.* **2018**, *8*, 4120−4131.
(16) Zhang, H.; Wang, X.; Frenkel, A. I.; Liu, P. Rationalization of Promoted Reverse Water Gas Shift Reaction by Pt3ni Alloy: Essential Contribution from Ensemble Effect. *J. Chem. Phys.* **2021**, *154*, No. 014702.
(17) Benzi, R.; Succi, S.; Vergassola, M. The Lattice Boltzmann Equation: Theory and Applications. *Phys. Rep.* **1992**, *222*, 145−197.
(18) Bokstein, B. S.; Mendelev, M. I.; Srolovitz, D. J. *Thermodynamics and Kinetics in Materials Science: A Short Course*; Oxford University Press: 2005; Vol. *1*.
(19) Che, S.; Lund, K.; Tatsumi, T.; Iijima, S.; Joo, S. H.; Ryoo, R.; Terasaki, O. Direct Observation of 3d Mesoporous Structure by Scanning Electron Microscopy (SEM): SBA-15 Silica and CMK-5 Carbon. *Angew. Chem., Int. Ed.* **2003**, *42*, 2182−5.
(20) Pekridis, G.; Kalimeri, K.; Kaklidis, N.; Vakouftsi, E.; Iliopoulou, E. F.; Athanasiou, C.; Marnellos, G. E. Study of the Reverse Water Gas Shift (RWGS) Reaction over Pt in a Solid Oxide Fuel Cell (SOFC) Operating under Open and Closed-Circuit Conditions. *Catal. Today* **2007**, *127*, 337−346.
(21) Garbarino, G.; Bellotti, D.; Riani, P.; Magistri, L.; Busca, G. Methanation of Carbon Dioxide on Ru/Al_2O_3 and Ni/Al_2O_3 Catalysts at Atmospheric Pressure: Catalysts Activation, Behaviour and Stability. *Int. J. Hydrogen Energy* **2015**, *40*, 9171−9182.
(22) Kresse, G.; Furthmuller, J. Efficient Iterative Schemes for Ab Initio Total-Energy Calculations Using a Plane-Wave Basis Set. *Phys. Rev. B Condens. Matter* **1996**, *54*, 11169−11186.
(23) Kresse, G.; Joubert, D. From Ultrasoft Pseudopotentials to the Projector Augmented-Wave Method. *Phys. Rev. B* **1999**, *59*, 1758−1775.
(24) Kresse, G.; Furthmüller, J. Efficiency of Ab-Initio Total Energy Calculations for Metals and Semiconductors Using a Plane-Wave Basis Set. *Comput. Mater. Sci.* **1996**, *6*, 15−50.
(25) Perdew, J. P.; Burke, K.; Ernzerhof, M. Generalized Gradient Approximation Made Simple. *Phys. Rev. Lett.* **1996**, *77*, 3865−3868.
(26) Press, W. H.; Flannery, B. P.; Teukolsky, S. A.; Vetterling, W. T. *Numerical Recipes: The Art of Scientific Computing*; Cambridge University Press: New York, 1986.
(27) Pulay, P. Convergence Acceleration of Iterative Sequences. The Case of Scf Iteration. *Chem. Phys. Lett.* **1980**, *73*, 393−398.
(28) Mills, G.; Jónsson, H.; Schenter, G. K. Reversible Work Transition State Theory: Application to Dissociative Adsorption of Hydrogen. *Surf. Sci.* **1995**, *324*, 305−337.
(29) Jónsson, H.; Mills, G.; Jacobsen, K. W. Nudged Elastic Band Method for Finding Minimum Energy Paths of Transitions. *Classical and Quantum Dynamics in Condensed Phase Simulations* **1998**, 385−404.
(30) Henkelman, G.; Jónsson, H. Improved Tangent Estimate in the Nudged Elastic Band Method for Finding Minimum Energy Paths and Saddle Points. *J. Chem. Phys.* **2000**, *113*, 9978−9985.

(31) Henkelman, G.; Uberuaga, B. P.; Jónsson, H. A Climbing Image Nudged Elastic Band Method for Finding Saddle Points and Minimum Energy Paths. *J. Chem. Phys.* **2000**, *113*, 9901−9904.
(32) Cortright, R. D.; Dumesic, J. A. Kinetics of Heterogeneous Catalytic Reactions: Analysis of Reaction Schemes. *Adv. Catal.* **2001**, *46*, 161−264.
(33) Liao, W.; Liu, P. Methanol Synthesis from Co2 Hydrogenation over a Potassium-Promoted $Cu_xO/Cu(111)$ ($x \leq 2$) Model Surface: Rationalizing the Potential of Potassium in Catalysis. *ACS Catal.* **2020**, *10*, 5723−5733.
(34) Santen, R. A.; Niemantsverdriet, J. W. *Chemical Kinetics and Catalysis (Fundamental and Applied Catalysis)*; Plenum Press: New York, 1995.
(35) Johnson, R. D., III, Ed. NIST Computational Chemistry Comparison and Benchmark Database, *NIST Standard Reference Database Number 101*, Release 22, May 2022; http://cccbdb.nist.gov/ .
(36) Chase, M. *NIST-JANAF Thermochemical Tables*, 4th ed.; American Institute of Physics: 1998, 1 (Accessed September 28, 2023).
(37) Arboleda, N. B.; Kasai, H.; Diño, W. A.; Nakanishi, H. Potential Energy of H2dissociation and Adsorption on Pt(111) Surface: First-Principles Calculation. *Jpn. J. Appl. Phys.* **2007**, *46*, 4233−4237.
(38) Kraus, P.; Frank, I. On the Dynamics of H_2 Adsorption on the Pt(111) Surface. *Int. J. Quantum Chem.* **2017**, *117*, e25407.
(39) Kresse, G. Dissociation and Sticking of H_2 on the Ni(111), (100), and (110) Substrate. *Phys. Rev. B* **2000**, *62*, 8295.
(40) Yang, H.; Whitten, J. L. Dissociative Adsorption of H_2 on Ni(111). *J. Chem. Phys.* **1993**, *98*, 5039−5049.
(41) Zheng, C. Z.; Yeung, C. K.; Loy, M. M.; Xiao, X. Quantum Diffusion of H on Pt(111): Step Effects. *Phys. Rev. Lett.* **2006**, *97*, 166101.
(42) Yamakawa, K; Hohler, B; Kronmuller, H Diffusion of Hydrogen in Nickel-Based Alloys. *J. Phys.: Condens. Matter* **1989**, *1*, 2031.
(43) Choi, Y.; Liu, P. Mechanism of Ethanol Synthesis from Syngas on Rh(111). *J. Am. Chem. Soc.* **2009**, *131*, 13054−13061.
(44) Grabow, L. C.; Gokhale, A. A.; Evans, S. T.; Dumesic, J. A.; Mavrikakis, M. Mechanism of the Water Gas Shift Reaction on Pt: First Principles, Experiments, and Microkinetic Modeling. *J. Phys. Chem. C* **2008**, *112*, 4608−4617.
(45) Hammer, B.; Nørskov, J. K. Theoritical Surface Science and Catalysis - Calculations and Concepts. *Adv. Catal.* **2000**, *45*, 71−129.
(46) Xin, H.; Vojvodic, A.; Voss, J.; Nørskov, J. K.; Abild-Pedersen, F. Effects of D-Band Shape on the Surface Reactivity of Transition-Metal Alloys. *Phys. Rev. B* **2014**, *89*, 115114.
(47) Ruban, A.; Hammer, B.; Stoltze, P.; Skriver, H. L.; Norskov, J. K. Surface Electronic Structure and Reactivity of Transition and Noble Metals. *J. Mol. Catal. A-Chem.* **1997**, *115*, 421−429.
(48) Takigawa, I.; Shimizu, K.-i.; Tsuda, K.; Takakusagi, S. Machine-Learning Prediction of the D-Band Center for Metals and Bimetals. *RSC Adv.* **2016**, *6*, 52587−52595.
(49) Zhao, X.; Xi, C.; Zhang, R.; Song, L.; Wang, C.; Spendelow, J. S.; Frenkel, A. I.; Yang, J.; Xin, H. L.; Sasaki, K. High-Performance Nitrogen-Doped Intermetallic Ptni Catalyst for the Oxygen Reduction Reaction. *ACS Catal.* **2020**, *10*, 10637−10645.

https://doi.org/10.1021/acs.jpcc.3c05655
J. Phys. Chem. C 2023, 127, 22067−22075